Available online at www.sciencedirect.com
ScienceDirect
Journal of Sound and Vibration 321 (2009) 184–200
JOURNAL OF SOUND AND VIBRATION
www.elsevier.com/locate/jsvi

Vibration control of maglev vehicles traveling over a flexible guideway

J.D. Yau*

Department of Architecture, Tamkang University, 5, Lane 199, Kinghua Street, Taipei 10620, Taiwan

Received 20 April 2008; received in revised form 10 August 2008; accepted 11 September 2008
Handling Editor: J. Lam
Available online 11 November 2008

Abstract

As a series of maglev (magnetically levitated) vehicles travel over a flexible guideway with constant speeds, their acceleration amplitudes will be amplified significantly at resonant or higher speeds. This paper intends to develop a neuro-PI (proportional-integral) controller to control the dynamic response of the maglev vehicles around an allowable prescribed acceleration. The maglev vehicle is simplified as a two-degree-of-freedom (two-dof) moving oscillator controlled by an on-board PI controller and the guideway is modeled as a simply supported beam. Considering the motion-dependent nature of electromagnetic forces working in a maglev system, this study presents an iterative approach to compute the dynamic response of a maglev-oscillator/guideway coupling system based on the Newmark method. The proposed neuro-PI controller is trained using back-propagation neural network in such a way that its PI gains are correlated to the generated data set of moving speeds, mid-span acceleration amplitude of the guideway, and maximum vertical accelerations of maglev oscillators. Numerical simulations demonstrate that a trained neuro-PI controller has the ability to control the acceleration amplitude for running maglev vehicles within an allowable region of prescribed acceleration.

1. Introduction

The commercial operation of the Shanghai maglev transport system in 2002 marked the beginning of a new era in maglev transport system. Compared with traditional wheel/track transit vehicles, a high-speed maglev train can offer the advantages of low energy consumption, less environmental impact, as well as lower noise and emissions. With the advanced maglev technology, powerful magnets are able to lift a vehicle up and propel it forward along a guideway via electromagnetic forces. According to the suspension modes to guide a maglev train moving on guideways, two kinds of maglev technologies have been developed: (1) electromagnetic suspension (EMS, see Fig. 1(a)) with attractive mode; (2) electrodynamic suspension (EDS, see Fig. 1(b)) with repulsive mode [1–3]. The EMS system can lift a train up using attractive forces by the magnets beneath a guide-rail. The EDS system suspends a train above its guide-rail using magnetic repulsive

*Tel.: +886 2 23581830; fax: +886 2 23959041.
E-mail address: jdyau@mail.tku.edu.tw

0022-460X/$ - see front matter © 2008 Elsevier Ltd. All rights reserved.
doi:10.1016/j.jsv.2008.09.030

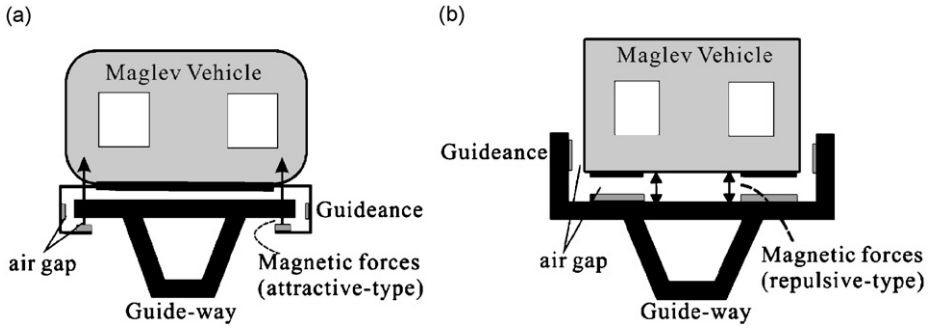

Fig. 1. Schematic diagram of two maglev-vehicle systems: (a) electromagnetic suspension (EMS) and (b) electrodynamic suspension (EDS).

forces to take the train off the U-shaped guideway. To suspend a maglev vehicle at a stable levitation gap (air gap) between the on-board levitation magnets and the guideway, a controllable electromagnetic field is generated in its maglev suspension system. Obviously, the response analysis of a maglev train moving on a flexible guideway is related to not only the dynamics of vehicle/guideway interaction but also the control of the maglev system.

With the recent development of high-speed rail in ground transportation, there are many literatures on the study of train-induced vibration of railway bridges [4–15]. One of the important findings in these research works is that as a train travels over a bridge at resonant speeds, the response of the bridge tends to increase steadily as there are more loads passing the bridge [5,6,9]. This is the so-called ''resonance phenomenon'' for rail bridges. However, relatively little research attention so far seems to conduct the dynamic interaction response of maglev trains running on guideways at resonant speeds. Cai and Chen [16] and Cai et al. [17] investigated the response characteristics of different maglev-vehicle models traveling over flexible guideways. They concluded that a concentrated-load vehicle model might result in larger responses of both guideway deflections and vehicle accelerations than a distributed-load vehicle model. In the literature review works conducted by Cai and Chen [18], various aspects of the dynamic characteristics, magnetic suspension systems, vehicle stability, and suspension control laws for maglev/guideway coupling systems were discussed. Zheng et al. [19,20] presented two kinds of vehicle/guideway coupling models with controllable magnetic suspension systems to investigate the vibration behavior of a maglev vehicle running on a flexible guideway. They observed the phenomena of divergence, flutter, and collision on the dynamic stability of a maglev-vehicle traveling on a flexible guideway. By simulating a magnetic force as an equivalent spring-dashpot system, Zhao and Zhai [21] modeled a TR06 carriage as a 10-degree-of-freedom (10 dof) vehicle model with a rigid car body supported by four sets of magnet bogies to investigate the vertical random response and ride quality of a maglev vehicle traveling on elevated guideways.

In this study, a simplified model of a two-dof maglev oscillator controlled by a PI controller [22–24] is employed to simulate a maglev vehicle moving on a flexible guideway. The guideway is modeled as a simply supported beam. Based on the maglev theory, the maglev-oscillator system is lifted up above the guideway with a stable levitation gap via a motion-dependent electromagnetic force (see Fig. 1). By employing Galerkin's method to convert the governing equations containing moving maglev oscillators into two sets of generalized differential equations, the computation of dynamic response for the vehicle/guideway coupling system was carried out using an iterative approach [15] with Newmark's β method [25]. To control the dynamic response of a series of maglev oscillators running on a flexible guideway with various speeds, a neuro-PI controller based on back-propagation algorithm [26,27] is developed, in which it can provide suitable control gains in reducing the response of maglev oscillators. Numerical simulations indicate that the dynamic response of maglev vehicles traveling over a flexible guideway at resonant speed can be restricted to a preset acceleration using the proposed neuro-PI controller.

2. Formulation

2.1. Basic considerations

Generally, the lateral flexural stiffness of a guideway is much larger than the vertical one. For this reason, the lateral vibrations of the guideway due to moving maglev vehicles will also be smaller than the vertical motions. To simplify the formulation of vehicle/guideway interaction with the maglev system, only vertical vehicle motion is considered in this study because it can dominate the dynamic behavior of vehicle/guideway interactions [17]. The following are the assumptions adopted for the maglev-vehicle/guideway system:

(1) The flexible guideway is modeled as a linear elastic Bernoulli–Euler beam with uniform cross-section.
(2) A maglev train passing over the guideway is modeled as a sequence of identical maglev vehicles with equal intervals.
(3) The maglev vehicle is modeled as a one-dimensional and two-dof oscillator model that consists of two concentrated masses, with the top one representing the mass lumped from the car body and the bottom one the mass of a magnetic wheel-set.
(4) The effect of time delay between the input voltage and the output current on a maglev suspension system is negligible.

2.2. Governing equations of motion

As shown in Fig. 2, a sequence of identical maglev oscillators with equal intervals d is crossing a single-span flexible guideway at constant speed v. The maglev-oscillator model is composed of a lumped mass (car body) supported by a spring-dashpot system connected with a magnet bogie, from which a controllable electromagnetic force is generated to lift the vehicle model up at a stable levitation gap. Here, we shall use the following symbols to denote the properties depicted in Fig. 2: m = mass of the guideway girder, c = damping coefficient, EI = flexural rigidity, m_1 = lumped mass of magnetic wheel-set, m_2 = lumped mass of car body, c_v = primarily damping coefficient, and k_v = primarily stiffness coefficient. The equation of motion for a simple beam carrying multiple moving oscillators is [9,15]

$$m\ddot{u}_d + c\dot{u}_d + \mathrm{EI}u''''_d = p(x,t), \tag{1}$$

$$p(x,t) = \sum_{k=1}^{N} G_k(i_k,h_k)\delta(x-x_k)[H(t-t_k) - H(t-t_k-L/v)] \tag{2}$$

with the following boundary conditions:

$$u_d(0,t) = u_d(L,t) = 0,$$
$$\mathrm{EI}u''_d(0,t) = \mathrm{EI}u''_d(L,t) = 0, \tag{3a,b}$$

where $(\bullet)' = \partial(\bullet)/\partial x$, $(\dot{\bullet}) = \partial(\bullet)/\partial t$, $u_d(x,\ t)$ = vertical deflection of the beam, p_0 = lumped weight of maglev vehicle = $(m_1+m_2)g$, g = gravity acceleration, $\delta(\bullet)$ = Dirac's delta function, $H(t)$ = unit step function, k = 1, 2, 3, …, Nth moving load on the beam, $t_k = (k-1)d/v$ = arrival time of the kth load into the beam, x_k = position of the kth load along the guideway, y_{1k} = vertical displacement of the kth lumped mass m_1 (magnetic wheel), and y_{2k} = vertical displacement of the kth lumped mass m_2 (car body). The equations of motion for the kth maglev oscillator with two-dofs are [4,9]

$$\begin{bmatrix} m_1 & 0 \\ 0 & m_2 \end{bmatrix}\begin{Bmatrix} \ddot{y}_{1k} \\ \ddot{y}_{2k} \end{Bmatrix} + \begin{bmatrix} c_v & -c_v \\ -c_v & c_v \end{bmatrix}\begin{Bmatrix} \dot{y}_{1k} \\ \dot{y}_{2k} \end{Bmatrix} + \begin{bmatrix} k_v & -k_v \\ -k_v & k_v \end{bmatrix}\begin{Bmatrix} y_{1k} \\ y_{2k} \end{Bmatrix} = \begin{Bmatrix} p_0 - G_k(i_k,h_k) \\ 0 \end{Bmatrix}. \tag{4}$$

Here, $G_k(i_k, h_k)$ denotes the control electromagnetic force between the magnetic wheel-set and the guideway, which is given by [2,3]

$$G_k(i_k,h_k) = K_0(i_k(t)/h_k(t))^2, \tag{5}$$

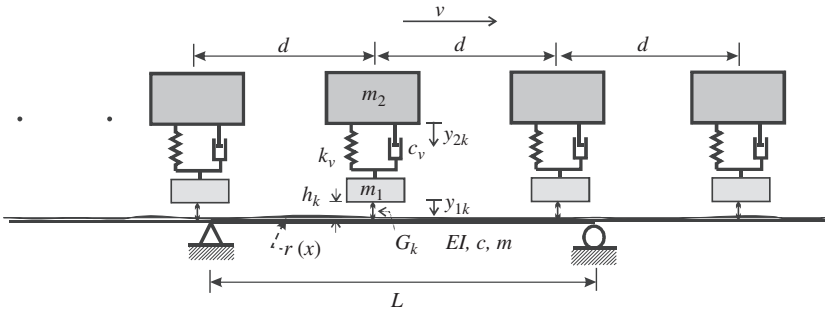

Fig. 2. A flexible guideway under moving maglev train loads.

where $K_0 = \mu_0 N_0^2 A_0/4 =$ coupling factor [1–3], $\mu_0 =$ vacuum permeability, $N_0 =$ number of turns of the magnet windings, $A_0 =$ pole face area, $i_k(t) = i_0 + \imath_k(t) =$ control current, $\imath_k(t) =$ deviation of control current, $h_k(t) = h_0 + y_{1k}(t) - u_d(x_k) + r(x_k) =$ levitation gap, $r(x) =$ irregularity of guideway, and $(i_0, h_0) =$ desired values of control current and levitation gap around a specified nominal operating point for a maglev wheel-set. By expressing the electromagnetic force in Eq. (4) in terms of the inertial forces of the maglev oscillator, one can obtain $G_k(i_k, h_k) = p_0 - m_1\ddot{y}_{1k} - m_2\ddot{y}_{2k}$. Considering the static equilibrium for the suspended maglev oscillator in Eq. (5) yields [19,20]

$$G_k(i_0, h_0) = K_0(i_0/h_0)^2 = (m_1 + m_2)g = p_0, \tag{6}$$

where the coupling factor K_0 is equal to $p_0(h_0/i_0)^2$. From the theory of electromagnetic circuits, the electromagnetic equation for the magnet current and control voltage in the kth maglev system is given by [1–3]

$$\Gamma_0 \frac{\mathrm{d}(i_k/h_k)}{\mathrm{d}t} + R_0 i_k = V_k, \tag{7}$$

where $\Gamma_0 = 2K_0 =$ initial inductance of the coil winding the suspension magnet, $R_0 =$ coil resistance of electronic circuit, and $V_k =$ control voltage. Let us adopt the variable transformation as $\gamma_k = i_k/h_k$, Eq. (7) can be rewritten as

$$\Gamma_0\dot{\gamma}_k + R_0 h_k(t)\gamma_k = V_k. \tag{8}$$

Consider the control error of $e_k = i_0/h_0 - i_k/h_k = \gamma_0 - \gamma_k$ for the parameter γ_k, the control voltage of V_k can be expressed using the PI tuning algorithm as [22–24]

$$V_k = K_p e_k + K_i \int_0^t e_k \,\mathrm{d}t, \tag{9}$$

where $K_p =$ proportional gain and $K_i =$ integral gain [22–24]. Then substituting Eq. (9) into Eq. (8) and differentiating this equation with respect to time, after some mathematical manipulation, one can achieve the following differential equation for control error:

$$\Gamma_0\ddot{e}_k + K_p\dot{e}_k + K_i e_k = R_0\dot{h}_k\gamma_0 - R_0(h_k\dot{e}_k + \dot{h}_k e_k). \tag{10}$$

Here, the nonlinear term of $-R_0(h_k\dot{e}_k + \dot{h}_k e_k)$ has been regarded as a *pseudo* excitation and removed to the right-hand side of the differential equation. Let us suppose the proportional gain K_p in Eq. (10) as a damping coefficient in a dynamic equation. Then one can use the concept of proportional damping to represent the proportional gain in terms of $(\Gamma_0,\ K_i)$ as $K_p = 2\zeta\sqrt{\Gamma_0 K_i}$ [9]. Here, $\zeta =$ equivalent damping ratio. Combining Eqs. (4) and (10) yields the following equation of motion for the kth maglev oscillator:

$$[m_v]\{\ddot{u}_{vk}\} + [c_v]\{\dot{u}_{vk}\} + [k_v]\{u_{vk}\} = \{f_{vk}\}, \tag{11}$$

where

$$\{u_{vk}\}=\begin{Bmatrix} y_{1k} \\ y_{2k} \\ e_k \end{Bmatrix},\quad [m_v]=\begin{bmatrix} m_1 & 0 & 0 \\ 0 & m_2 & 0 \\ 0 & 0 & \Gamma_0 \end{bmatrix},\quad [c_v]=\begin{bmatrix} c_v & -c_v & 0 \\ -c_v & c_v & 0 \\ -R_0\gamma_0 & 0 & 2\zeta\sqrt{\Gamma_0 K_i} \end{bmatrix}, \tag{12a–c}$$

$$[k_v]=\begin{bmatrix} k_v & -k_v & -2p_0/\gamma_0 \\ -k_v & k_v & 0 \\ 0 & 0 & K_i \end{bmatrix},\quad \{f_{vk}\}=\begin{Bmatrix} -p_0(e_k/\gamma_0)^2 \\ 0 \\ R_0\gamma_0[\dot{r}(x_k)-\dot{u}_d(x_k)]-R_0[h_k\dot{e}_k+\dot{h}_k e_k] \end{Bmatrix}. \tag{12d,e}$$

To solve the nonlinear dynamic coupling equations shown in Eqs. (1), (2), (11) and (12), an incremental-iterative procedure will be presented in Section 3.

3. Applications of the incremental-iterative approach

According to the homogeneous boundary conditions shown in Eqs. (3) for a simple beam, the guideway deflection (u_d) can be expressed as follows [10]:

$$u_d(x,t)=\sum_{n=1} q_n(t)\sin\frac{n\pi x}{L}, \tag{13}$$

where $q_n(t)$ means the generalized coordinate associated with the nth assumed mode of the simple beam. From the coupling equations in Eqs. (1) and (11), the substitution of Eq. (13) into Eq. (1) and the application of Galerkin's method [10,14] may yield the following equations of motion for the nth generalized system of the guideway associated with the kth vehicle equation:

$$\begin{bmatrix} m & 0 \\ 0 & [m_v] \end{bmatrix}\begin{Bmatrix} \ddot{q}_n \\ \{\ddot{u}_{vk}\} \end{Bmatrix}+\begin{bmatrix} c & 0 \\ 0 & [c_v] \end{bmatrix}\begin{Bmatrix} \dot{q}_n \\ \{\dot{u}_{vk}\} \end{Bmatrix}+\begin{bmatrix} k_n & 0 \\ 0 & [k_v] \end{bmatrix}\begin{Bmatrix} q_n \\ \{u_{vk}\} \end{Bmatrix}=\begin{Bmatrix} p_n \\ \{f_{vk}\} \end{Bmatrix}, \tag{14}$$

where $k_n=\mathrm{EI}(n\pi/L)^4$, and the generalized force p_n is

$$\begin{aligned} &p_n=\sum_{k=1}^{N}[F_k(\varpi_n,v,t)-F_{vk}(\varpi_n,v,t)],\\ &F_k(\varpi_n,v,t)=\frac{2p_0}{L}\psi_n(\varpi_n,t),F_{vk}(\varpi_n,v,t)=\frac{2[m_1\ddot{y}_{1k}+m_2\ddot{y}_{2k}]}{L}\psi_n(\varpi_n,t),\\ &\psi_n(\varpi_n,t)=\sin\varpi_n(t-t_k)[H(t-t_k)-H(t-t_k-L/v)]. \end{aligned} \tag{15a – d}$$

Here, $\varpi_n=n\pi v/L=$ driving frequency of vehicle loads to the guideway [9].

To compute the nonlinear dynamic responses of both the maglev oscillators and the guideway, an iterative method is used in numerical simulation. With respect to the total responses of ($q_{n,t+\Delta t}$, $\dot{q}_{n,t+\Delta t}$, $\ddot{q}_{n,t+\Delta t}$) and ($\{u_{vk,t+\Delta t}\},\{\dot{u}_{vk,t+\Delta t}\},\{\ddot{u}_{vk,t+\Delta t}\}$) in Eq. (11) at time $t+\Delta t$, one can use Newmark's β method [9] to relate them to their responses at time t as

$$\begin{aligned} &q_{n,t+\Delta t}=q_{n,t}+\Delta q_n,\\ &\dot{q}_{n,t+\Delta t}=\dot{q}_{n,t}+a_6\ddot{q}_{n,t}+a_7\ddot{q}_{n,t+\Delta t},\\ &\ddot{q}_{n,t+\Delta t}=a_0\Delta q_n-a_2\dot{q}_{n,t}-a_3\ddot{q}_{n,t} \end{aligned} \tag{16a – c}$$

and

$$\begin{aligned} &\{u_{vk,t+\Delta t}\}=\{u_{vk,t}\}+\{\Delta u_{vk}\},\\ &\{\dot{u}_{vk,t+\Delta t}\}=\{\dot{u}_{vk,t}\}+a_6\{\ddot{u}_{vk,t}\}+a_7\{\ddot{u}_{vk,t+\Delta t}\},\\ &\{\ddot{u}_{vk,t+\Delta t}\}=a_0\{\Delta u_{vk}\}-a_2\{\dot{u}_{vk,t}\}-a_3\{\ddot{u}_{vk,t}\} \end{aligned} \tag{17a – c}$$

with the following integration constants [9,25]:

$$a_0 = \frac{1}{\beta\Delta t^2}, \quad a_1 = \frac{\gamma}{\beta\Delta t}, \quad a_2 = \frac{1}{\beta\Delta t}, \quad a_3 = \frac{1}{2\beta} - 1, \quad a_4 = \frac{\gamma}{\beta} - 1,$$
$$a_5 = \frac{\Delta t}{2}\left(\frac{\gamma}{\beta} - 2\right), \quad a_6 = (1-\gamma)\Delta t, \quad a_7 = \gamma\Delta t \qquad (18a - h)$$

and $\beta = 0.25$ and $\gamma = 0.5$. Then the equivalent stiffness equations for the incremental step from time t to $t+\Delta t$ with the feature of *iteration* are written by [15]

$$K_{n,\mathrm{eq}} \times \Delta q^{i}_{n,t+\Delta t} = \Delta p^{i-1}_{n,t+\Delta t}, [K_{v,eq}]\{\Delta u^{i}_{vk,t+\Delta t}\} = \{\Delta f^{i-1}_{vk,t+\Delta t}\}, \qquad (19a,b)$$

where $i =$ iterative number, and the equivalent stiffness terms of $K_{n,\mathrm{eq}}$ and $[K_{v,\mathrm{eq}}]$ are

$$K_{n,\mathrm{eq}} = a_0 m + a_1 c + k_n, [K_{v,\mathrm{eq}}] = a_0[m_v] + a_1[c_v] + [k_v] \qquad (20a,b)$$

and $(\Delta p^{i-1}_{n,t+\Delta t}, \{\Delta f^{i-1}_{vk,t+\Delta t}\})$ are interpreted as the *unbalanced forces* during the following iterative steps. The unbalanced force $\Delta p^{i-1}_{n,t+\Delta t}$ is equal to the difference between the external force $p^{i-1}_{n,t+\Delta t}$

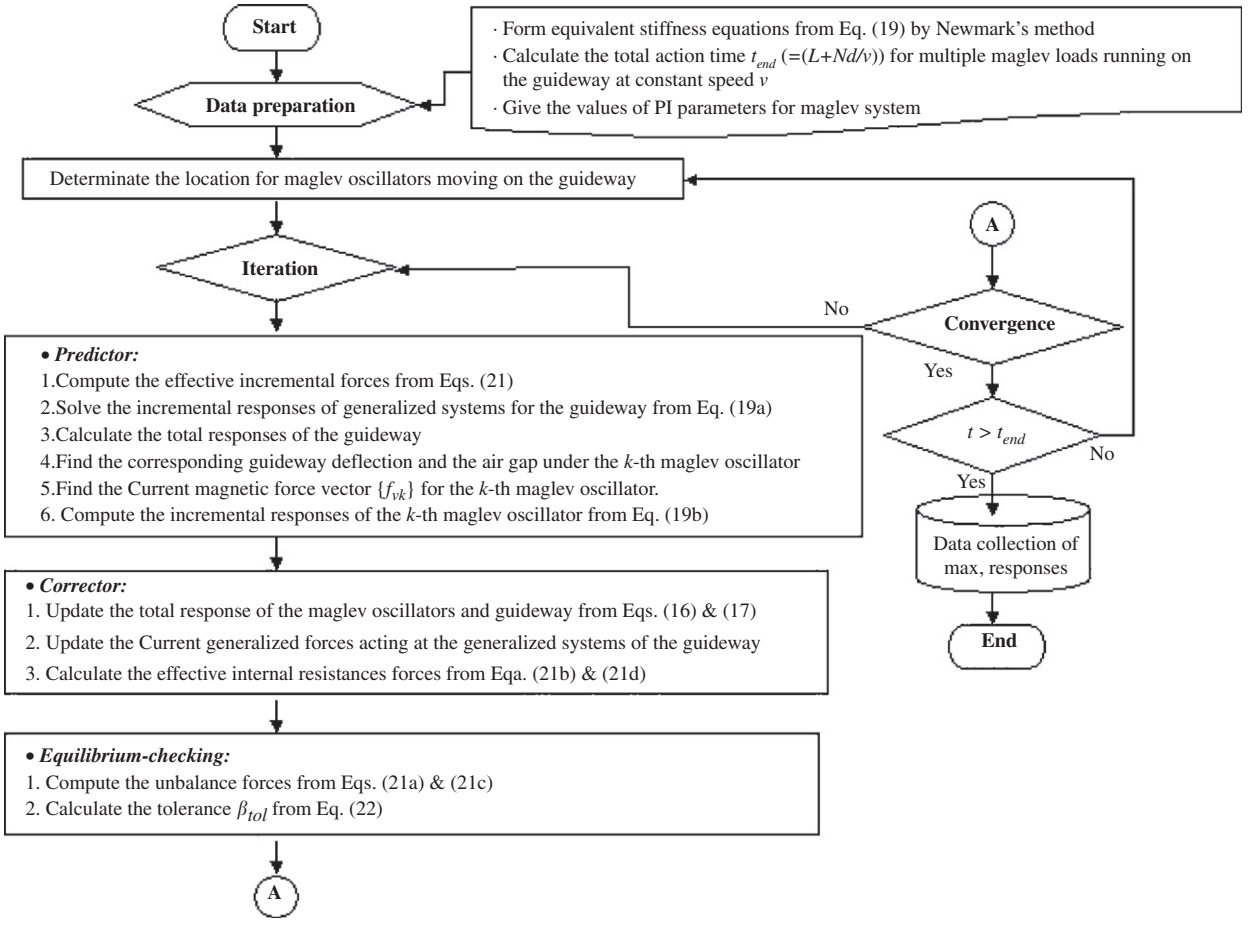

Fig. 3. Flow chart of the incremental-iterative procedure.

and the effective internal forces $f^{i-1}_{n,t+\Delta t}$ for the nth generalized system of the simple beam at time $t+\Delta t$, i.e.,

$$\Delta p^{i-1}_{n,t+\Delta t} = p^{i-1}_{n,t+\Delta t} - f^{i-1}_{n,t+\Delta t},$$
$$f^{i-1}_{n,t+\Delta t} = \begin{cases} k_n q^{i-1}_{n,t+\Delta t} - m(a_2\dot{q}^{i-1}_{n,t+\Delta t} + a_3\ddot{q}^{i-1}_{n,t+\Delta t}) - c(a_4\dot{q}^{i-1}_{n,t+\Delta t} + a_5\ddot{q}^{i-1}_{n,t+\Delta t}) & \text{for } i=1, \\ k_n q^{i-1}_{n,t+\Delta t} + m\ddot{q}^{i-1}_{n,t+\Delta t} + c\dot{q}^{i-1}_{n,t+\Delta t} & \text{for } i>1. \end{cases} \quad (21a,b)$$

Similarly, the unbalanced force vector $\{\Delta f^{i-1}_{vk,t+\Delta t}\}$ and the effective internal force vector $\{r^{i-1}_{vk,t+\Delta t}\}$ for the kth maglev oscillator at time $t+\Delta t$ are

$$\{\Delta f^{i-1}_{vk,t+\Delta t}\} = \{f^{i}_{vk,t+\Delta t}\} - \{r^{i-1}_{vk,t+\Delta t}\},$$
$$\{r^{i-1}_{vk,t+\Delta t}\} = \begin{cases} [k_v]\{u^{i-1}_{vk,t+\Delta t}\} - [m_v](a_2\{\dot{u}^{i-1}_{vk,t+\Delta t}\} + a_3\{\ddot{u}^{i-1}_{vk,t+\Delta t}\}) & \text{for } i=1, \\ \quad -[c_v](a_4\{\dot{u}^{i-1}_{vk,t+\Delta t}\} + a_5\{\ddot{u}^{i-1}_{vk,t+\Delta t}\}) & \\ [k_v]\{u^{i-1}_{vk,t+\Delta t}\} + [m_v]\{\ddot{u}^{i-1}_{vk,t+\Delta t}\} + [c_v]\{\dot{u}^{i-1}_{vk,t+\Delta t}\} & \text{for } i>1. \end{cases} \quad (21c,d)$$

The flow chart for incremental-iterative dynamic analysis including the three phases, predictor, corrector, and equilibrium checking, has been outlined in Fig. 3. The predictor phase is concerned with the solution of the structural response increments of $(\Delta q^{i}_{n,t+\Delta t}, \{\Delta u^{i}_{vk,t+\Delta t}\})$ for given loadings $(\Delta p^{i-1}_{n,t+\Delta t}, \{\Delta f^{i-1}_{vk,t+\Delta t}\})$ from the equivalent stiffness equations; the corrector phase relates to the recovery of the internal resistant forces $(f^{i-1}_{n,t+\Delta t}, \{r^{i-1}_{vk,t+\Delta t}\})$ from the displacement increments of $(\Delta q^{i}_{n,t+\Delta t}, \{\Delta u^{i}_{vk,t+\Delta t}\})$ and the total responses of $(q^{i}_{n,t+\Delta t}, \dot{q}^{i}_{n,t+\Delta t}, \ddot{q}^{i}_{n,t+\Delta t})$ and $(\{u^{i}_{vk,t+\Delta t}\}, \{\dot{u}^{i}_{vk,t+\Delta t}\}, \{\ddot{u}^{i}_{vk,t+\Delta t}\})$ made available in the predictor; the equilibrium-checking phase is used to calculate the unbalanced forces $(\Delta p^{i-1}_{n,t+\Delta t}, \{\Delta f^{i-1}_{vk,t+\Delta t}\})$ from the differences between the effective internal forces $(f^{i-1}_{n,t+\Delta t}, \{r^{i-1}_{vk,t+\Delta t}\})$ and the external loads $(p^{i-1}_{n,t+\Delta t}, \{f^{i-1}_{vk,t+\Delta t}\})$. Whenever the root mean square of the sum of the generalized unbalanced forces, that is,

$$\beta_{\text{tol}} = \left[\sum\nolimits_{k=1\ldots}(\Delta f^{i-1}_{vk,t+\Delta t})^2 + \sum\nolimits_{n=1\ldots}(\Delta p^{i-1}_{n,t+\Delta t})^2\right]^{1/2} \quad (22)$$

is larger than a preset tolerance, say 10^{-3}, iteration for removing the unbalanced forces involving the two phases of the predictor and the corrector should be repeated.

4. Applications of back-propagation network to pi controllers

Using a PI controller to control a structure, one needs to tune the PI gains so that its output can exhibit an oscillation behavior through the process of trial and error [22]. In this section, an artificial neural network (ANN) model based on back-propagation learning algorithm is proposed to determine the PI gains for a controlled maglev vehicle. The present PI controller with a trained ANN will be called a neuro-PI controller. A back-propagation network (BPN) with feed-forward architecture has been widely applied to various engineering areas for its simplicity and straightforward nature [26,27].

The BPN model is trained using the supervised learning algorithm and its basic architecture (see Fig. 3) includes three layers of processing units: input layer, hidden layer, and output layer. Among these layers, they are interconnected with the neurons that each of them is linked via weighted connections. Here, $\mathbf{W}_o$ and $\mathbf{W}_h$ are the weighted matrices of the output and hidden layers, respectively. The input phase is to feed information to the neural network system through the neurons of the input layer. Then, each neuron of the hidden and output layers processes its input by multiplying its weight through a nonlinear activation function. The sigmoid function of $f(x) = 1(1+e^{-x})$ is chosen as the activation function of the BPN model for its

differentiability and continuity, i.e., $df(x)/dx = f(x)(1-f(x))$, which is rather easy to calculate when performing the gradient steepest procedure using the back-propagation algorithm. The error between the target outputs and the predicted results is iteratively minimized through the weights adjusted at each training cycle in the neural network computations. The error function is defined by the following half-sum of squared error:

$$E_r = \frac{1}{2}\sum_j (T_j - Y_j)^2, \tag{23}$$

where T_j = target output for pattern "j", Y_j = predicted output. Here, the predicted output Y_j is defined as follows:

$$Y_j = f(x_j), \quad x_j = \sum_i (w_{ij} Y_i - b_j), \tag{24}$$

where w_{ij} denotes the connective weight between neurons i and j and b_i is the bias associated with the jth neuron of the hidden layer. To minimize the error function E_r, the present BPN model adopts the following weight update rule [27]:

$$\Delta w_{ij}(k+1) = -\eta \frac{\partial E_r}{\partial w_{ij}} + \alpha \Delta w_{ij}(k), \tag{25}$$

where k = learning cycle, η = learning rate, and α = momentum term. The momentum term is used to avoid oscillation problems and to keep the training process stable by treating the previous weight change of $\Delta w_{ij}(k)$ as a parameter of the new weight change of $\Delta w_{ij}(k+1)$. Once the target outputs (training phase) and the predicted results (testing phase) are found to be in good agreement with each other, the output predictions from the trained BPN model can produce reliable output results for the inputs within the range of the training set (Fig. 4).

To determine the PI gains from a trained BPN model, let us denote $a_{g,\max}$ as the maximum mid-span acceleration of the guideway and $a_{v,\max}$ as the maximum vertical acceleration of the moving maglev oscillators. Considering different pairs of PI gains in maglev systems, the dynamic response analysis of vehicle/guideway interaction can be carried out using the incremental-iterative procedure presented in Section 3. Then the generated information of (v, $a_{v,\max}$, $a_{g,\max}$, K_p, K_i) are collected as an initial off-line learning database to train the proposed BPN model for predicting the control gains of neuro-PI controllers. In this study, three parameters (v, $a_{g,\max}$, and $a_{v,\max}$) are used as the input patterns to feed the BPN learning model while the PI gains of (K_p, K_i) as the output predictions.

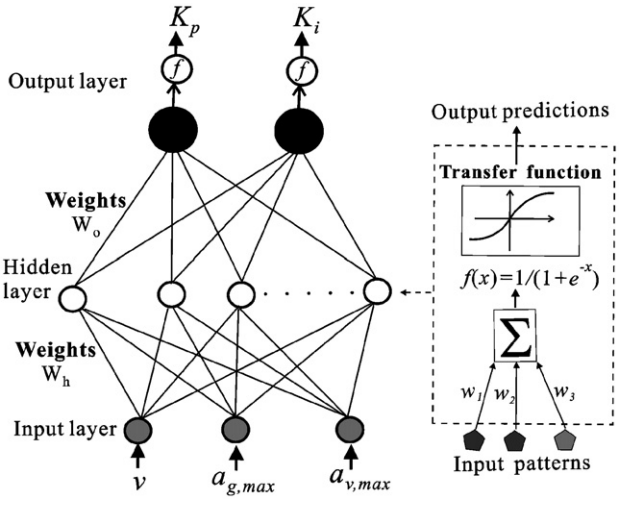

Fig. 4. Architecture of a typical three-layered neural network.

5. Numerical verifications

Fig. 2 shows a series of identical maglev oscillators with equal intervals d crossing a single-span guideway at constant speed v. It was well known that if the *acceleration response*, rather than the displacement response, of a simple beam is of concern, higher modes have to be included in the computation [15]. In this study, the first 16 modes of shape functions are employed to compute the acceleration response of the simply supported guideway and two-dof maglev oscillators by using the time step of 0.001 s and the ending time of $t_{end} = (L + Nd)/v$.

Moreover, to account for the random nature and characteristics of guide-rail irregularity in practice, the following *power spectrum density* function [9] is given to simulate the vertical profile of guideway geometry variations:

$$S(\Omega) = \frac{A_v \Omega_c^2}{(\Omega^2 + \Omega_r^2)(\Omega^2 + \Omega_c^2)}, \tag{26}$$

where Ω = spatial frequency, and A_v ($= 1.5 \times 10^{-7}$ m), Ω_r ($= 2.06 \times 10^{-6}$ rad/m), and Ω_c ($= 0.825$ rad/m) are relevant parameters. Fig. 5 shows the vertical profile of track irregularity for the simulation of guide-rail geometry variations in this study.

5.1. Response for a maglev vehicle traveling on a single-span concrete guideway

For the purpose of verification for the proposed maglev-vehicle/guideway interaction model, a TR06 maglev vehicle is treated as an eight-set of two-dof sprung mass systems with equal intervals ($d = 3$ m), as shown in Fig. 2. The main data for the TR06 maglev vehicle with length 24 m and a single-span concrete guideway with span 24.854 m [21,32] are given as follows: $EI = 24.56 \times 10^6$ kN m^2, $m = 3760$ kg/m, $m_1 = 4000$ kg, $m_2 = 3700$ kg, $c_v = 10.6$ kN s/m, $k_v = 85$ kN/m, $h_0 = 8$ mm, $i_0 = 37$ A, and $R_0 = 1.10\,\Omega$. Let the maglev oscillators travel on the smooth guideway with a constant speed of 400 km/h. Considering three pairs of adjusted PI gains, i.e., ($K_i = 6.0$, $K_p = 0.01$), ($K_i = 6.0$, $K_p = 0.03$), and ($K_i = 7.0$, $K_p = 0.01$), the time history responses for mid-span guideway deflection and the vertical acceleration of the first maglev oscillator, together with the numerical results obtained from Ref. [21], have been plotted in Figs. 6 and 7, respectively. They indicate that the proposed vehicle/guideway model with PI gains of ($K_i = 6.0$, $K_p = 0.01$) has the ability to simulate the dynamic behavior of a TR06 maglev vehicle running on a concrete guideway. From the

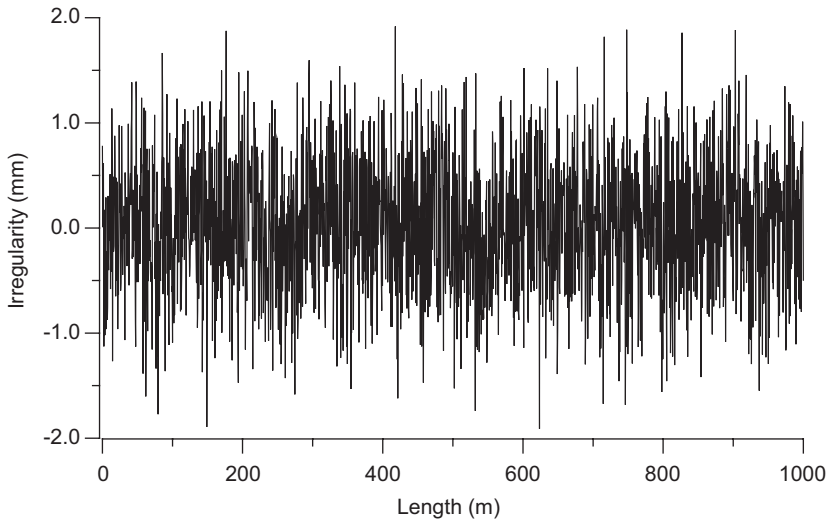

Fig. 5. Guide-rail irregularity (vertical profile).

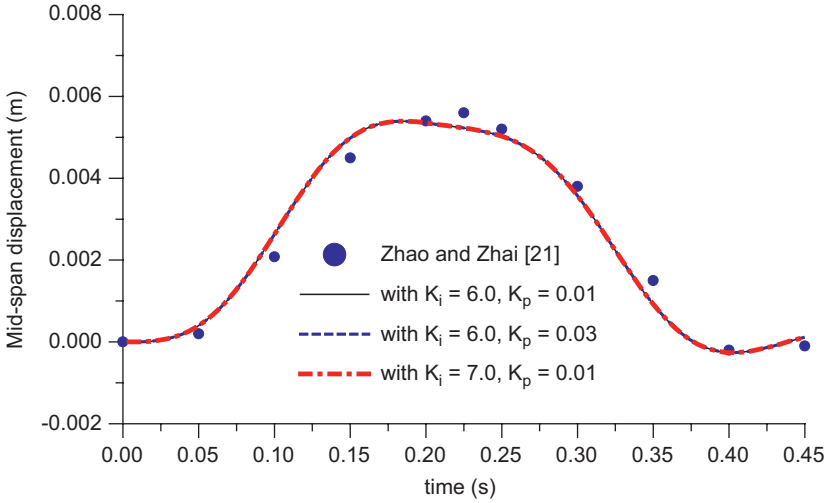

Fig. 6. Time history response of mid-span displacement.

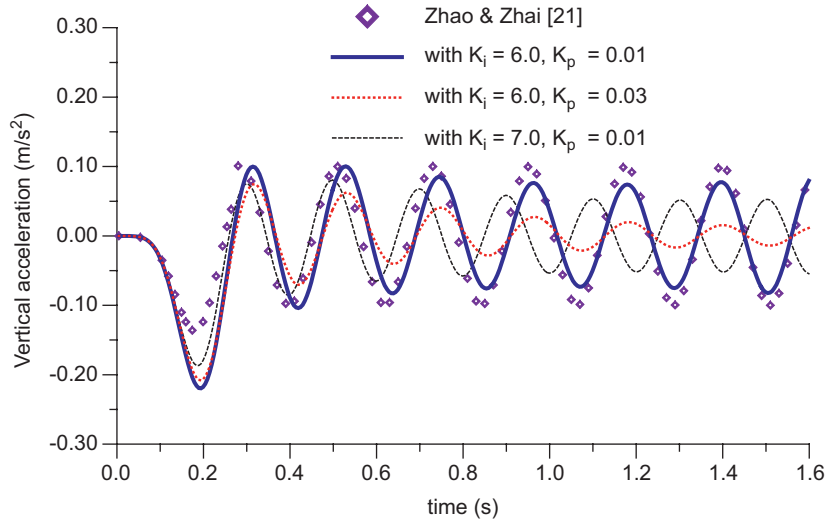

Fig. 7. Time history response of vertical acceleration for maglev oscillators.

Table 1
Properties and natural frequency of the guideway

L (m)	EI (N m^2)	m (kg/m)	c (N s/m/m)	f_0[a] (Hz)	v_{res} (km/h)
30	7.9×10^{10}	1.5×10^4	3.77×10^4	4	360

[a] f_0 = the fundamental frequency of the guideway.

response curves in Fig. 6, little difference exists between the acceleration responses of the guideway subject to the three types of moving maglev oscillators. The reason is that the inertia force of $(m_1\ddot{y}_{1k} + m_2\ddot{y}_{2k})$ induced by a moving maglev oscillator is much lower than its static load (p_0) acting at the guideway [17]. From the response curves in Fig. 7, the larger proportional gain is helpful to mitigate the response amplitude of the maglev oscillator and the integral gain plays the role of energy dissipation to damp out the residual vibration of the moving maglev vehicle after passing through the guideway.

Table 2
Properties of the maglev oscillator

N	d (m)	p_0 (N)	m_1 (kg)	m_2 (kg)	c_v (N s/m)	k_v (N/m)	h_0 (m)	i_0 (A)	R_0 (Ω)	Γ_0 (m^2 H)
12	25	1.28×10^5	3×10^3	10^4	1.5×10^4	3×10^5	0.01	25	0.8	0.041

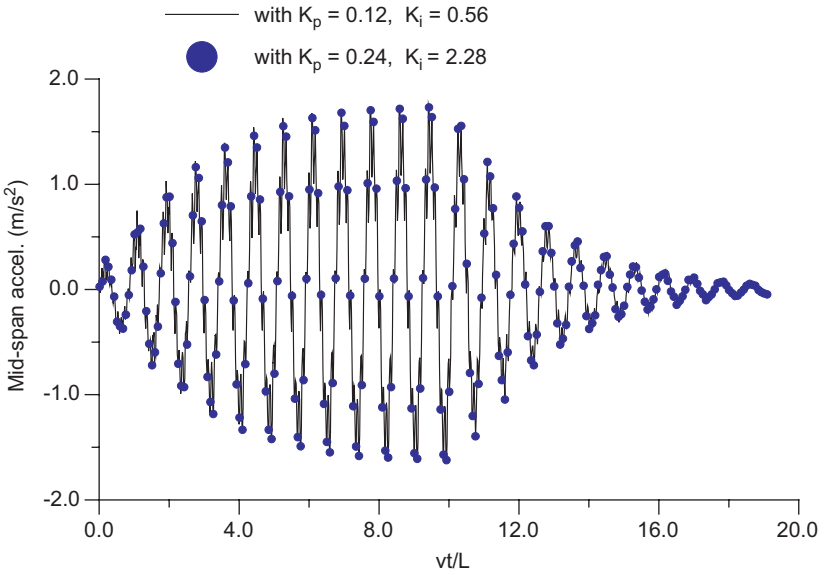

Fig. 8. Resonant response of mid-span acceleration of the guideway.

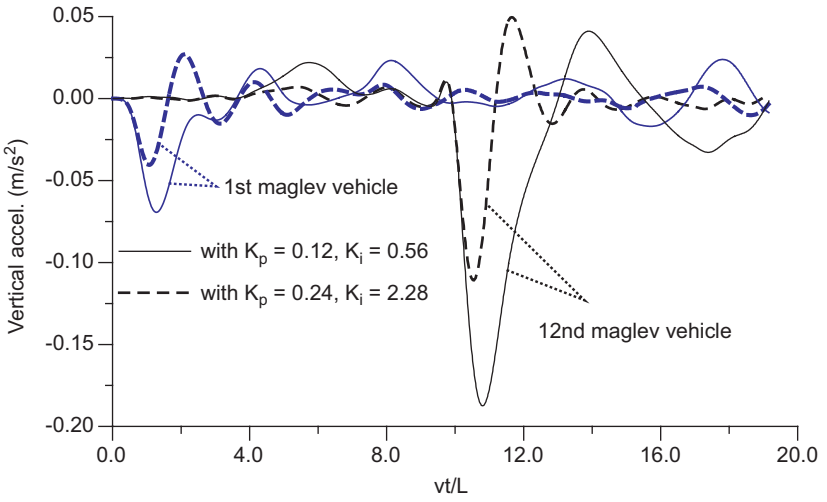

Fig. 9. Vertical acceleration responses of maglev oscillators.

5.2. *Resonance response of a flexible guideway*

As a series of moving loads with equal intervals (d) travel over a bridge at the resonant speed $v_{res} = f_0 d$, the dynamic response of the bridge will build up continuously as there are more vehicular loads passing through

the bridge [10–15]. To demonstrate this resonance phenomenon, let us consider the dynamic model (the EDS system) in Fig. 2 with the properties of the guideway and maglev oscillator shown in Tables 1 and 2. Two pairs of constant PI gains, i.e., ($K_p = 0.12$, $K_i = 0.56$) and ($K_p = 0.24$, $K_i = 2.28$), are selected for the controlled maglev oscillators, respectively. Fig. 8 shows the time history responses of mid-span acceleration of the guideway induced by the two types of maglev oscillators moving at resonant speed. Fig. 9 depicts the vertical acceleration responses of the sprung masses (m_2) for the first and the last ($N = 12$) maglev oscillators. Since the guideway response shown in Fig. 8 is built up continuously as there are more moving loads passing through the guideway, the last maglev oscillator entering the vibrating guideway in resonance just right experiences the portion of larger vertical guideway excitations than the first one and its response is also amplified significantly. Of interest in the vehicle responses is the fact that the acceleration amplitude of a controlled maglev oscillator with larger PI gains is significantly smaller than that with smaller PI gains since a controller with larger control gains can offer more control efforts in mitigating the response of a vibrating oscillator.

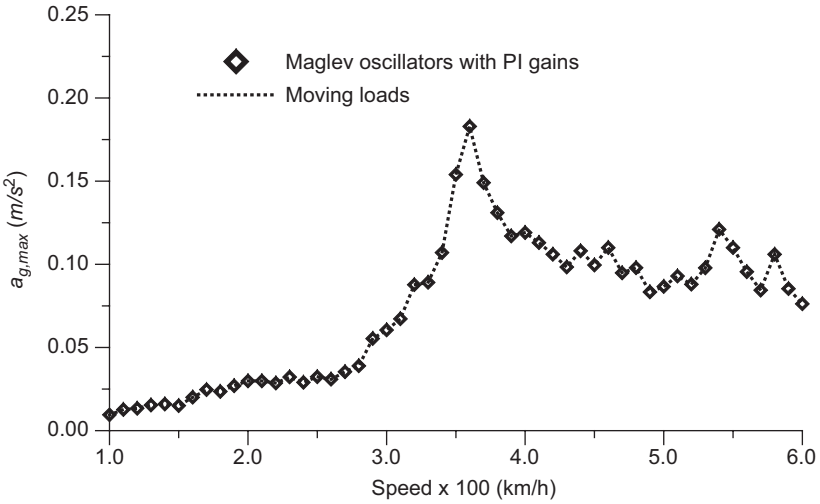

Fig. 10. Generated database of $a_{g,\max}-v$ vs. PI gains.

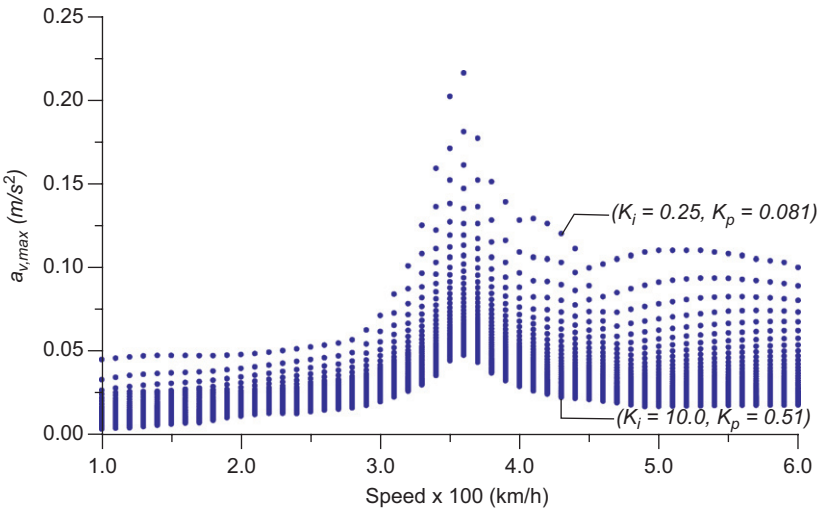

Fig. 11. Generated database of $a_{v,\max}-v$ vs. PI gains.

5.3. Training and testing of the proposed BPN model

In this study, the response curve of the maximum mid-span acceleration ($a_{g,\max}$) of the guideway vs. moving speed (v) is denoted as the $a_{g,\max}-v$ plot and the maximum vertical acceleration ($a_{v,\max}$) of the maglev oscillators vs. moving speed as the $a_{v,\max}-v$ plot. For the purpose of training the BPN learning model, this study uses the data set of (v, $a_{v,\max}$, $a_{g,\max}$) as three input patterns and the control gains of (K_p, K_i) as two output predictions. Prior to the preparation of the learning database, an equivalent damping ratio (ζ) of a neuro-PI controller is set to 0.4 for the proportional parameter $K_p(=2\zeta\sqrt{\Gamma_0 K_i})$ and the integral gain K_i ranges from 0.25 to 10 with a step size of 0.25. Let the maglev oscillators travel over the guideway with speeds (v) from 100 to 600 km/h with an increment of 10 km/h. Figs. 10 and 11 show the distribution of the $a_{g,\max}-v$ plot and the $a_{v,\max}-v$ plot, in which the entire database of (v, $a_{v,\max}$, $a_{g,\max}$, K_p, K_i) is carried out by computing the nonlinear analysis procedure of vehicle/guideway interaction response shown in Section 3. Since the inertia forces of moving maglev oscillators acting on the guideway are much lower than their static loads, the coupling effects of vehicle/guideway have littlie difference [17] on the $a_{g,\max}-v$ plots shown in Fig. 10. From Fig. 11, peak amplitudes in the $a_{v,\max}-v$ plots still exist at the resonant speed of 360 km/h even for the maglev oscillators with the largest PI gains ($K_p = 0.51$, $K_i = 10$).

With the training database depicted in Figs. 10 and 11, 2040 data patterns are generated and collected from the present computing results, in which the total data pairs are used as training data while a subset of 1020 data pairs randomly selected from the total data set is used to test the prediction capability of the trained BPN model. To obtain the *simplest* BPN model that can fit the present study of interest, a basic training strategy is outlined as follows [27–31]: (1) the increase of hidden layers may produce complex error surfaces and raise the possibility containing local minima, but the more hidden units can increase the accuracy of output predictions; (2) a BPN learning model with a single hidden layer and sufficient neurons is capable of providing an approximate but accurate solution of practical interest; and (3) the use of Gaussian-based random initial database and a noise factor (0.01) in the updating weights can help avoid possible local minima on the error surface during the training process. Considering the BPN parameters of $\eta = 0.95$, $\alpha = 0.5$, and $k = 1000$ for the weight updating equation given in Eq. (25) and trying different combinations for the number of neurons in the hidden layer based on the previous training strategy, this study adopted a three (input pattern):16 (hidden neuron): two (output prediction) three-layered BPN architecture with a convergent rate of 0.03. Fig. 12 depicts the scattering diagrams of the predicted data set vs. the target data set for testing PI gains (K_i, K_p), in which the

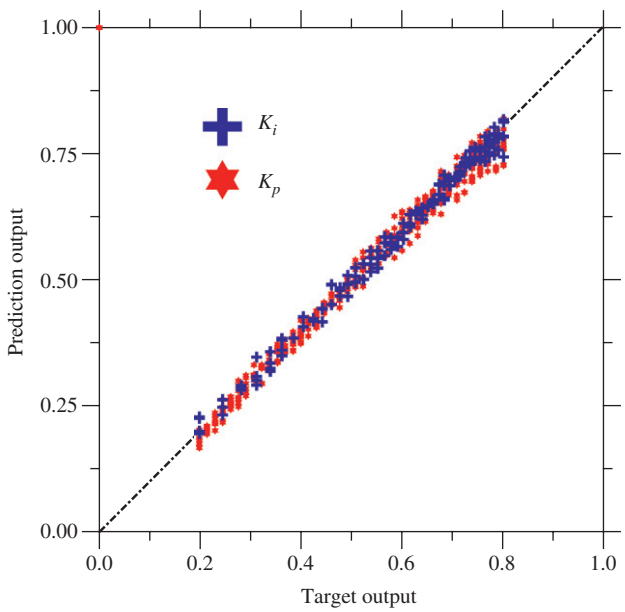

Fig. 12. Scattering correlation diagram for target and predicted outputs.

correlation coefficient is defined as

$$\rho = \frac{\sum_{i=1}^{n}(T_i - \bar{T})(P_i - \bar{P})}{(n-1)\sigma_T \sigma_P}, \tag{27}$$

where T means the symbol for target data and P for predicted data; $n =$ number of predicted data, $(\bar{T}, \bar{P}) =$ average value, and$\sigma =$ standard deviation. The scattering diagram shows that the correlation data are uniformly distributed along the diagonal line for the PI gains, from which the predicted outputs are quite close to the target ones.

To verify the prediction capability of the trained BPN model, one pair of *constant* PI parameters ($K_p = 0.24$, $K_i = 2.28$) used in Section 5.2 is selected as the actual PI gains for the maglev system of controlled maglev oscillators. The data set of (v, $a_{v,\max}$, $a_{g,\max}$) is utilized as the input patterns to feed the trained BPN model. Then the predicted PI gains (K_p, K_i) learned from the present BPN model were generated and are plotted in Fig. 13. Generally, the plot of the predicted outputs vs. speed is distributed irregularly around the constant PI parameters ($K_p = 0.24$, $K_i = 2.28$) since the BPN model searched for a pair of *optimal* PI gains that can achieve the minimum vertical acceleration response of maglev oscillators from the input patterns. A comparison of the $a_{v,\max}-v$ plot for the maglev vehicles controlled by the actual PI controllers with that by the trained neuro-PI controllers has been shown in Fig. 14. It can be seen that the predicted response curve of the $a_{v,\max}-v$ plot agrees very well with the target one.

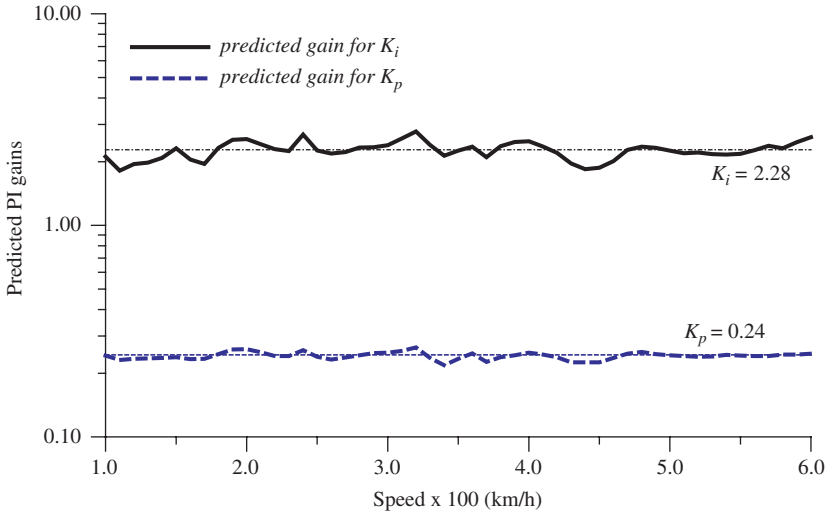

Fig. 13. Output predictions of PI gains vs. speeds.

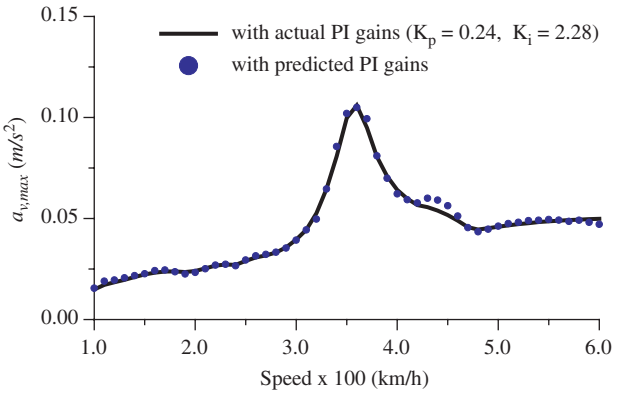

Fig. 14. Simulation of the $a_{v,\max}-v$ plot for trained neuro-PI controllers.

5.4. Performance of the proposed BPN model

As illustrated in Example 5.3, the increase of PI gains (K_p, K_i) for a controlled maglev system is helpful to mitigate the dynamic response of moving maglev vehicles. But the peak amplitude at the resonant speed of 360 km/h still exists in the $a_{v,\max}-v$ plot for maglev vehicles. In addition, to ensure the ride quality and running safety of maglev vehicles, acceleration amplitudes are needed to be restricted. For these reasons, let us restrict the maximum acceleration amplitude of moving maglev oscillators to a preset acceleration amplitude ($a_{v,\mathrm{rst}}$). Then the data set of (v, $a_{g,\max}$, $a_{v,\mathrm{rst}}$) is used as input patterns to feed the trained BPN model for yielding a specific data set of predicted PI gains that can change its control parameters along with moving speeds to satisfy the requirement of the preset acceleration. In this example, two cases of restricted accelerations, say, 0.05 and 0.10 m/s^2, are employed to verify the prediction capability of the trained BPN model. Under the two restricted acceleration amplitudes, the predicted values of (K_i, K_p) against moving speeds for the trained neuro-PI controllers have been depicted in Fig. 15, respectively. The output predictions of PI gains indicate that both

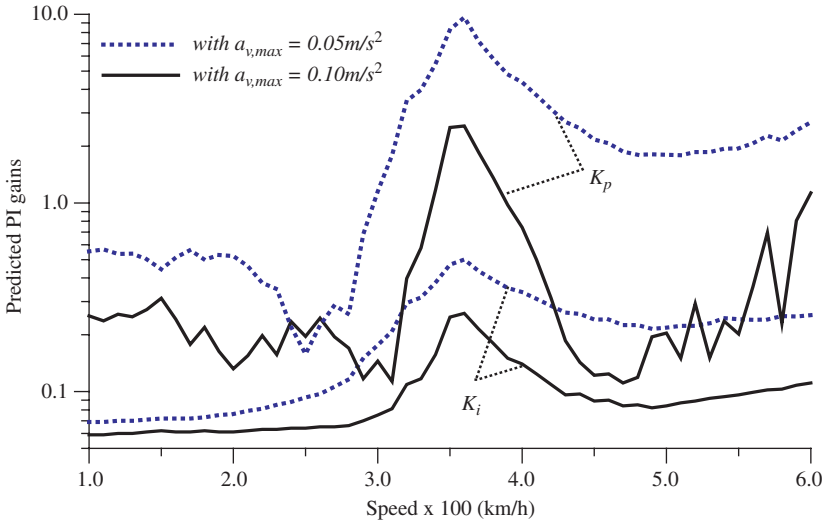

Fig. 15. Output predictions of PI gains vs. speeds.

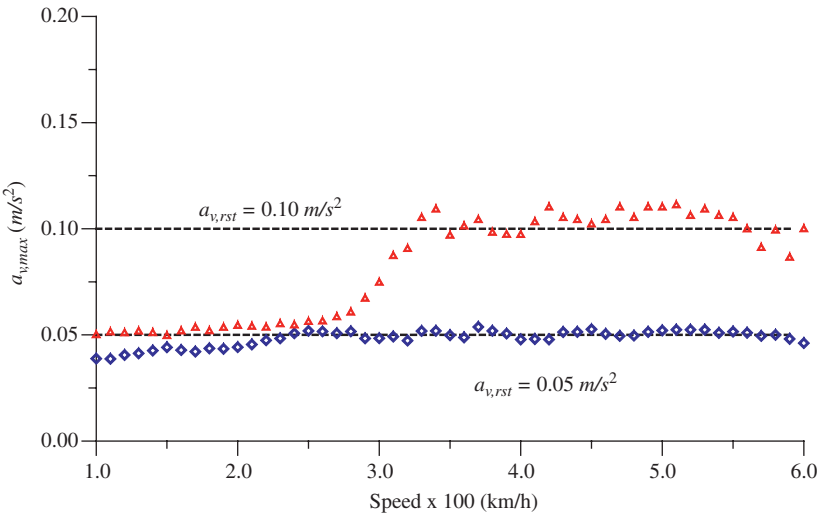

Fig. 16. $a_{v,\max}-v$ plots with preset restricted accelerations.

the predicted PI gains of (K_i, K_p) may reach their maximum at the resonant speed of 360 km/h. It means that the maglev vehicles moving at resonant speed require more control efforts to keep the vehicle responses around the restricted acceleration ($a_{v,\mathrm{rst}}$). Meanwhile, the distribution of the predicted $a_{v,\max}-v$ plots shown in Fig. 16 indicates that both the peak acceleration amplitudes for the maglev oscillators have been effectively controlled within an allowable region determined by the prescribed requirement. On the other hand, as moving speeds are lower than 300 km/h, the most maximum acceleration amplitudes are around 0.05 m/s^2 for the case of $a_{v,\mathrm{rst}} = 0.10\,\mathrm{m/s^2}$ since the corresponding PI gains shown in the training database of $a_{v,\max}-v$ plots in Fig. 10 are able to offer enough control forces to maintain the vertical acceleration response of maglev oscillators within the prescribed maximum acceleration.

6. Concluding remarks

In this study, the nonlinear dynamic analysis for a maglev-vehicle/guideway coupling system with PI controllers was carried out using an incremental-iterative procedure involving three phases of *predictor*, *corrector*, and *equilibrium checking*. Based on the present study, some observation on the vibration control of maglev vehicles traveling over a guideway using the proposed neuro-PI controller can be drawn as follows:

(1) As the *passage frequencies* (v/d) caused by a series of moving maglev oscillators coincides with the natural frequency of a guideway, larger responses will be developed on both the maglev vehicles and the guideway at this resonant speed.
(2) The numerical examples demonstrate that the proposed neuro-PI controller can reasonably simulate the control behavior of an actual PI controller for the maglev oscillators moving on a flexible guideway.
(3) To restrict the peak accelerations for maglev vehicles around a prescribed acceleration amplitude, the proposed neuro-PI controller has the ability to change its control gains along with moving speeds to satisfy the requirement based on ride quality and running safety of maglev vehicles.
(4) Even though the allowable bound of acceleration to be restricted for maglev oscillators is over the acceleration amplitudes in training database for some moving speeds, the proposed neuro-PI controller has the ability to search a set of *available* PI gains that can offer enough control forces to control the acceleration response of maglev oscillators within the allowable region of the prescribed acceleration.

Acknowledgements

The research reported herein was supported in part by grants from the National Science Council of the ROC through no. NSC 97-2221-E-032-022-MY2.

References

[1] P.K. Sinha, *Electromagnetic Suspension, Dynamics and Control*, Peter Peregrinus Ltd., London, UK, 1987.
[2] A. Bittar, R.M. Sales, H_2 and H_∞ control for maglev vehicles, *IEEE Control Systems Magazine* 18 (4) (1998) 18–25.
[3] D.L. Trumper, S.M. Olson, P.K. Subrahmanyan, Linearizing control of magnetic suspension systems, *IEEE Transactions on Control Systems Technology* 5 (4) (1997) 427–438.
[4] L. Frýba, *Vibration of Solids and Structures under Moving Loads*, third ed., Thomas Telford, London, 1999.
[5] Y.B. Yang, J.D. Yau, L.C. Hsu, Vibration of simple beams due to trains moving at high speeds, *Engineering Structures* 19 (1997) 936–944.
[6] S.H. Ju, H.T. Lin, Resonance characteristics of high-speed trains passing simply supported bridges, *Journal of Sound and Vibration* 267 (2003) 1127–1141.
[7] S.H. Ju, H.T. Lin, Numerical investigation of a steel arch bridge and interaction with high-speed trains, *Engineering Structures* 25 (2003) 241–250.
[8] H. Xia, N. Zhang, G. De Roeck, Dynamic analysis of high speed railway bridge under articulated trains, *Computers and Structures* 81 (2003) 2467–2478.
[9] Y.B. Yang, J.D. Yau, Y.S. Wu, *Vehicle–Bridge Interaction Dynamics*, World Scientific, Singapore, 2004.
[10] J.D. Yau, Y.B. Yang, Vertical accelerations of simple beams due to successive loads traveling at resonant speeds, *Journal of Sound and Vibration* 289 (2006) 210–228.

[11] J.D. Yau, Vibration of parabolic tied-arch beams due to moving loads, *International Journal of Structural Stability and Dynamics* 6 (2006) 193–214.
[12] J.D. Yau, Vibration of arch bridges due to moving loads and vertical ground motions, *Journal of Chinese Institute of Engineers* 29 (2006) 1017–1027.
[13] J.D. Yau, L. Fryba, Response of suspended beams due to moving loads and vertical seismic ground excitations, *Engineering Structures* 29 (2007) 3255–3262.
[14] J.D. Yau, Train-induced vibration control of simple beams using string-type tuned mass dampers, *Journal of Mechanics* 23 (4) (2007) 329–340.
[15] J.D. Yau, Y.B. Yang, Vibration of a suspension bridge installed with a water pipeline and subjected to moving trains, *Engineering Structures* 30 (2008) 632–642.
[16] Y. Cai, S.S. Chen, Numerical analysis for dynamic instability of electrodynamic maglev systems, *Shock and Vibration* 2 (1995) 339–349.
[17] Y. Cai, S.S. Chen, D.M. Rote, H.T. Coffey, Vehicle/guideway dynamic interaction in maglev systems, *Journal of Dynamic Systems, Measurement, and Control—Transactions of the ASME* 118 (1996) 526–530.
[18] Y. Cai, S.S. Chen, Dynamic characteristics of magnetically-levitated vehicle systems, *Applied Mechanics Reviews—Transactions of the ASME* 50 (11) (1997) 647–670.
[19] X.J. Zheng, J.J. Wu, Y.H. Zhou, Numerical analyses on dynamic control of five-degree-of-freedom maglev vehicle moving on flexible guideways, *Journal of Sound and Vibration* 235 (2000) 43–61.
[20] X.J. Zheng, J.J. Wu, Y.H. Zhou, Effect of spring non-linearity on dynamic stability of a controlled maglev vehicle and its guideway system, *Journal of Sound and Vibration* 279 (2005) 201–215.
[21] C.F. Zhao, W.M. Zhai, Maglev vehicle/guideway vertical random response and ride quality, *Vehicle System Dynamics* 38 (3) (2002) 185–210.
[22] K.J. Astrom, T. Hagglund, *Automatic Tuning of PID Controllers*, Instrument Society of America, 1988.
[23] K. Ogata, *Modern Control Engineering*, third ed., Prentice-Hall International Inc., Englewood Cliffs, NJ, 1997.
[24] E. Poulin, A. Pomerleau, PI settings for integrating processes based on ultimate cycle information, *IEEE Transactions on Control Systems Technology* 7 (4) (1999) 509–511.
[25] N.M. Newmark, A method of computation for structural dynamics, *Journal of Engineering Mechanics Division—ASCE* 85 (1959) 67–94.
[26] J. Ghaboussi, A. Joghataie, Active control of structures using neural networks, *Journal of Engineering Mechanics—ASCE* 121 (4) (1995) 555–567.
[27] M.H. Hassoun, *Fundamentals of Artificial Neural Networks*, MIT Press, Cambridge, 1995.
[28] R. Hecht-Nielsen, Theory of the back propagation neural network, *Proceedings of the International Joint Conference on Neural Networks*, Vol. 1, IEEE Press, New York, 1989, pp. 593–605.
[29] K. Hornik, Approximation capabilities of multiplayer feed-forward networks, *Neural Networks* 4 (2) (1991) 251–257.
[30] A. Lunia, K.M. Isaac, K. Chandrashekhara, S.E. Watkins, Aerodynamic testing of a smart composite wing using fiber-optic strain sensing and neural networks, *Smart Materials and Structures* 9 (6) (2000) 767–773.
[31] M.J. Atalla, D.J. Inman, On model updating using neural networks, *Mechanical Systems and Signal Processing* 12 (1998) 135–161.
[32] G. Bohn, G. Steinmetz, The electromagnetic levitation and guidance technology of the Transrapid test facility Emsland, *IEEE Transactions on Magnetics* 20 (5) (1984) 1666–1671.